ARTICLE

Hierarchical 3D Architectured Ag Nanowires Shelled with NiMn-Layered Double Hydroxide as an Efficient Bifunctional Oxygen Electrocatalyst

Soressa Abera Chala, Meng-Che Tsai,* Wei-Nien Su,* Kassa Belay Ibrahim, Balamurugan Thirumalraj, Ting-Shan Chan, Jyh-Fu Lee, Hongjie Dai,* and Bing-Joe Hwang*

Read Online

ACCESS | 📊 Metrics & More | 📄 Article Recommendations | 🔵 Supporting Information

ABSTRACT: Herein, we report hierarchical 3D NiMn-layered double hydroxide (NiMn-LDHs) shells grown on conductive silver nanowire (Ag NWs) cores as efficient, low-cost, and durable oxygen reduction reaction (ORR)/oxygen evolution reaction (OER) bifunctional electrocatalysts for metal−air batteries. The hierarchical 3D architectured Ag NW@NiMn-LDH catalysts exhibit superb OER/ORR activities in alkaline conditions. The outstanding bifunctional activities of Ag NW@NiMn-LDHs are essentially attributed to increasing both site activity and site populations. The synergistic contributions from the hierarchical 3D open-pore structure of the LDH shells, improved electrical conductivity, and small thickness of the LDHs shells are associated with more accessible site populations. Moreover, the charge transfer between Ag cores and metals of LDH shells and the formation of defective and distorted sites (less coordinated Ni and Mn sites) strongly enhance the site activity. Thus, Ag NW@NiMn-LDH hybrids exhibit a 0.75 V overvoltage difference between ORR and OER with excellent durability for 30 h, demonstrating the distinguished bifunctional electrocatalyst reported to date. Interestingly, the homemade rechargeable Zn−air battery using the hybrid Ag NW@NiMn-LDHs (1:2) catalyst as the air electrode exhibits a charge−discharge voltage gap of ∼0.77 V at 10 mA cm^{-2} and shows excellent cycling stability. Thus, the concept of the hierarchical 3D architecture of Ag NW@NiMn-LDHs considerably advances the practice of LDHs toward metal−air batteries and oxygen electrocatalysts.

KEYWORDS: oxygen electrocatalyst, vacancy defects, hierarchical core−shell, nanostructure, silver nanowires, layered double hydroxides
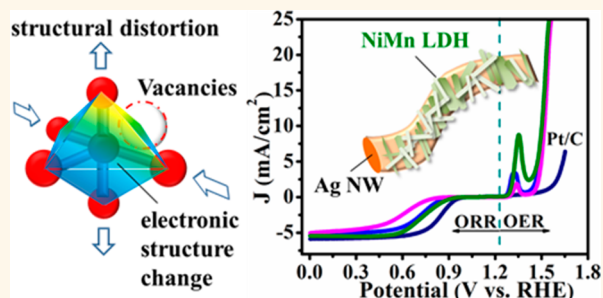
The demand for renewable and sustainable clean energy has inspired intense research on energy storage and conversion systems that are cost-effective, durable, and highly efficient catalysts to decrease fossil-fuel consumption and environmental impacts.[1,2] The oxygen reduction reaction (ORR) and oxygen evolution reaction (OER) are the crucial enablers of numerous renewable energy associated applications, such as energy storage through rechargeable metal−air batteries[2,3] and hydrogen generation *via* water splitting. These applications pledge sustainable and clean energy storage and conversion technologies.

The energy storage capacity of a Zn−air battery is rigorously constrained by the sluggish kinetics of the OER/ORR since both require four-proton and four-electron transfers to produce/reduce oxygen molecules. The slow process of ORR/OER leads to high overpotential, low efficiency, and considerable energy loss of the devices.[4,5] As a result, to improve energy efficiency and minimize the energy barrier, highly efficient and resourceful OER/ORR catalysts are required. The preeminent catalyst known to date for ORR is Pt-based material, while IrO_2 and RuO_2 are the OER benchmark catalysts.[3,6] However, their sources are not sustainable and are expensive, and consequently inappropriate for large-scale applications. Extensive research endeavors have been thus committed to the development of economically pleasing OER and ORR electrocatalysts including oxides of
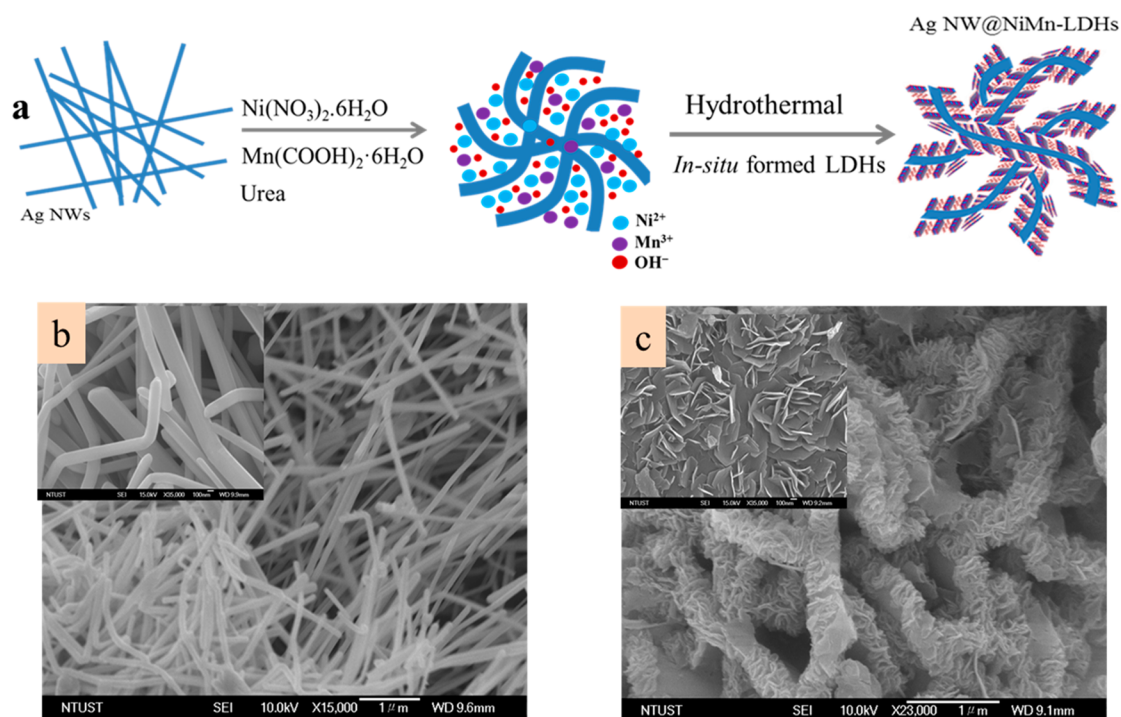
Figure 1. (a) Schematic fabrication process of hierarchical 3D architectured Ag NW@NiMn-LDH hybrids. (b) SEM images of the as-prepared Ag NWs and (c) hierarchical 3D architectured Ag NW@NiMn-LDH hybrids. The insets in (b and c) show high-magnification SEM images.
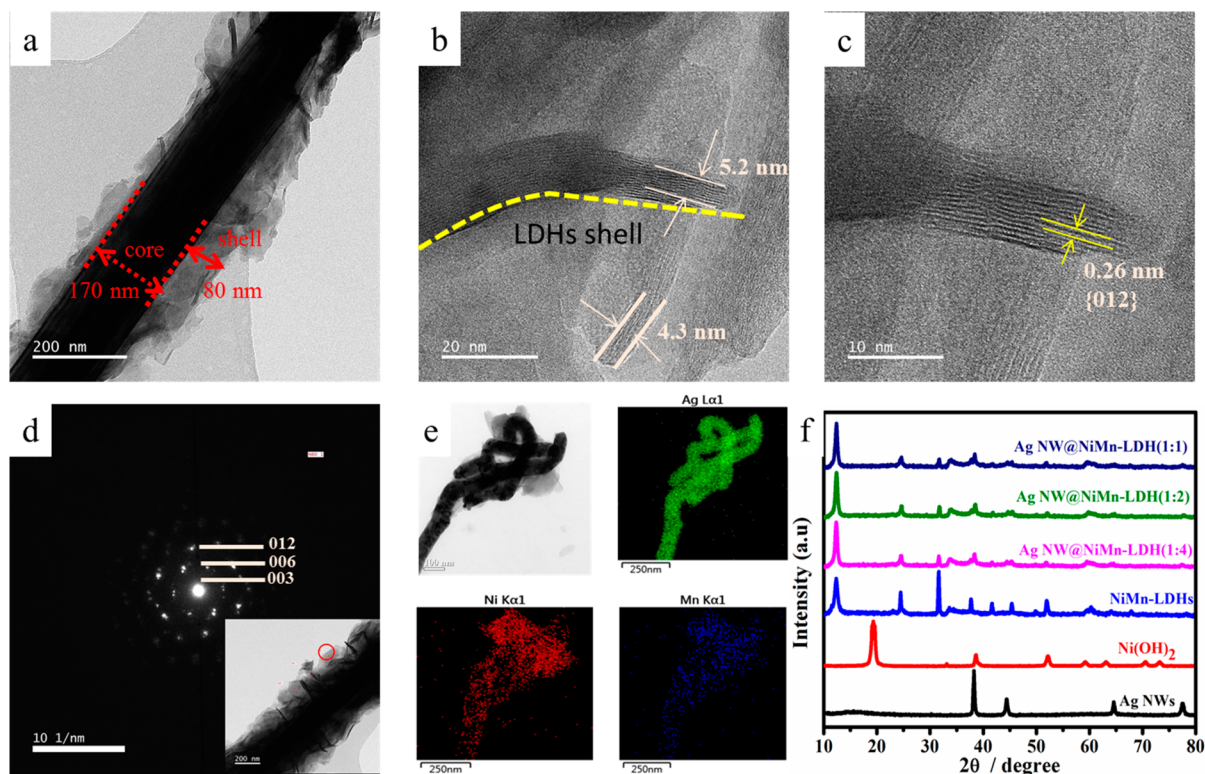

Figure 2. (a) TEM and (b, c) HR-TEM images of the hierarchical 3D architectured Ag NW@NiMn-LDHs hybrid. (d) Electron diffraction patterns of the Ag NW@NiMn-LDHs(1:2) hybrid marked in the inset of (d) and (e) TEM image and the corresponding elemental mapping images of Ag, Ni, and Mn atoms. (f) XRD patterns of Ag NWs, Ni(OH)$_2$, NiMn-LDHs, and Ag NW@NiMn-LDHs core−shell nanosheets with different feeding molar ratios of M salts (M = Ni, Mn) and Ag NWs.

transition metals,[2,7] perovskites,[8] carbon materials,[9] layered double hydroxides (LDHs),[10] nickel borate composites,[11,12]

and cobalt phosphate composites.[13,14] Among them, Ni-based oxides or hydroxides appear as efficient OER catalysts due to

their ease of scalability and abundant source.[7] Although many of them are OER active in alkaline conditions, they are ORR inactive.

Specifically, the OER activity of NiFe-LDHs is promising and exceeds the activity of Ir/C and IrO_2 catalysts. Nevertheless, the intrinsically poor electrical conductivity of LDHs and easily degradable active sites due to material stacking greatly prevent them from replacing precious metal electrocatalysts. One fruitful strategy for improvement is to integrate LDHs with highly conductive substrates such as carbon nanotubes, graphene oxide, and conductive metal.[15−17] NiFe-LDHs with highly conductive matrices (*e.g.* reduced graphene oxide[18,19] and carbon nanotubes[20]) have been extensively scrutinized, and the OER activity is superior to known noble metal catalysts (*e.g.*, IrO_2 and RuO_2[20]), which are crucial components for several energy conversion and storage processes.[21] While incorporating other transition metal species or conductive material might offer better activities of OER,[20,22,23] their ORR activity is less studied so far.[24]

Inspired by excellent electrical conductivity and the enormous surface area of Ag nanowires (NWs) and the electronically active character of Mn and Ni atoms, it is believed that the composite of Ag NWs cores and NiMn-LDHs shells can be a promising electrocatalyst for OER and ORR activities. Herein, we have intended and successfully developed hierarchical 3D architecture NiMn-LDHs nanosheet shells grown on highly conductive Ag NWs cores, denoted as Ag NW@NiMn-LDHs. The hierarchical 3D architectured Ag NW@NiMn-LDH hybrids exhibited marvelous activity with an OER onset overpotential of 0.19 and 0.27 V for ORR, which is superior to the performance of most nickel-based catalysts reported so far. The obtained Ag NW@NiMn-LDHs electrocatalyst has been tested for a rechargeable Zn−air battery and shows excellent performance.

RESULTS AND DISCUSSION

Figure 1a demonstrates a schematic diagram of the fabrication process of hierarchical 3D architectured Ag NW@NiMn-LDHs *via* the facile hydrothermal approach. The scanning electron microscopy (SEM) image (Figure 1b and the inset) reveals that the as-synthesized 1D Ag NWs have a uniform length, which can facilitate LDH coating. As illustrated in Figure S1a,b, the SEM images of the as-prepared pristine NiMn-LDHs reveal flower-like interconnected nanosheets and a porous morphology. These nanosheets have minimal self-aggregation and an open structure, which is advantageous for increasing the site populations of the catalytic reactions. The morphology and core−shell nanostructure of the Ag NW@NiMn-LDHs revealed by SEM clearly show that the hierarchical NiMn-LDHs architecture is composed of curved nanosheets vertically grown on the surface of conductive Ag NWs cores uniformly after hydrothermal reaction (Figure 1c, the inset in 1c, and Figure S1c,d). Energy-dispersive X-ray spectrometry (EDS) integrated with SEM presented in Figure S2 confirmed that the molar ratio of Ni/Mn in NiMn-LDHs is 3:1 and Ag/M (M = Ni,Mn) is 1:2 for the hybrid Ag NW@NiMn-LDHs(1:2) core−shell, which is close to the feeding ratio in the preparation.

Transmission electron microscopy (TEM) and high-resolution transmission electron microscopy (HR-TEM) further confirm the core−shell hierarchical structure of Ag NW@NiMn-LDH hybrids (Figure 2a). From the HR-TEM image (Figure 2b), the thickness of the LDH shell is

determined to be ∼4.3 to 5.2 nm. A single layer of LDHs has a thickness of 0.8 nm, and our Ag NW@NiMn-LDHs(1:2) has about 5 to 6 layers. Such a 3D architecture of a core−shell nanostructure with a few-layer hierarchical LDH shell would be anticipated to maximize the surface area and enable more active edge sites to be exposed, thus promoting the catalytic activity. A distinctive lattice fringe with an interplanar spacing of 0.26 nm (Figure 2c) was also identified, which can be assigned to the (012) plane of NiMn-LDHs. The electron diffraction patterns shown in Figure 2d clearly displayed the Debye−Scherrer rings, which can be indexed to the 003, 006, and 012 planes of LDHs. In addition, energy-dispersive X-ray measurement (EDX) elemental mapping (Figure 2e and Figure S3) shows that Ni and Mn elements are uniformly dispersed on the surface of Ag cores and entirely overlapped on one another. These results demonstrate that Ag nanowire cores are successfully embedded with NiMn-LDH shells to form a hierarchical 3D architectured Ag NW@NiMn-LDHs hybrid.

The X-ray diffraction (XRD) patterns of Ag NW@NiMn-LDH hybrids were indexed, and the crystal planes of all diffraction peaks corresponding to the typical layered structure of hydrotalcite-like materials and the superimposition of Ag NWs and NiMn-LDHs patterns were also observed (Figure 2f and Figure S4a). This indicates that the integration of NiMn-LDHs shells and the inner Ag NWs compositions was attained with high purity and crystallinity. The XRD patterns of Ag NW@NiMn-LDH hybrids showed slightly different *d*-spacing for crystal planes of (003) and (006) as the ratios of metal salts and Ag NWs varied from 1:1 to 1:4 (Figure S4b and Table S1). In addition, the thickness of the shells was estimated from the peak width of (003) and (006) crystal planes, which is ∼3.21 nm for Ag NW@NiMn-LDHs(1:2), lower than the estimated values of pristine NiMn-LDHs (∼3.75 nm). A single layer of LDHs has a thickness of 0.8 nm, and our Ag NW@NiMn-LDHs(1:2) has about 4 layers, while the pristine NiMn-LDHs has around 5 layers. The small thickness of LDHs shells would be anticipated to favor better OH^-/O_2 transport through the core−shell hybrids and increase accessible site populations.

The N_2-adsorption−desorption measurements were employed to understand the structure, surface area, and pore sizes of the hierarchical 3D architecture of Ag NW@NiMn-LDH hybrids. As shown in Figure S5a, the hysteresis loops of the measured N_2 isotherms at the relative pressure ($P/P_0 > 0.4$) indicate the adsorption−desorption processes of porous materials. The Brunauer−Emmett−Teller (BET) surface area of the hierarchical 3D nanostructure of Ag NW@NiMn-LDHs(1:2) is 162.4 m^2 g^{-1}, higher than that of Ag NW@NiMn-LDHs(1:4) (148.3 m^2 g^{-1}) and pristine NiMn-LDHs (61.8 m^2 g^{-1}). The growth of the vertically oriented hierarchical nanostructure of LDH shells on the surface of silver nanowires with less structural restacking and open-pore structure is beneficial to offer a high surface area of the hybrids. Such a high surface area and hierarchical 3D nanostructure of Ag NW@NiMn-LDHs(1:2) would provide more accessible active sites for the electrocatalytic process. The Barrett−Joyner−Halenda (BJH) pore size distribution obtained from the N_2 desorption reveal the hierarchical structure of the fabricated hybrid materials with pore diameters in the range between 5 and 20 nm (Figure S5b). The pore size distribution of pristine NiMn-LDHs is relatively wider than other samples.

FT-IR spectra (Figure S6) reveal that anions such as OH^-, H_2O molecules, and CO_3^{2-} anions are fully intercalated
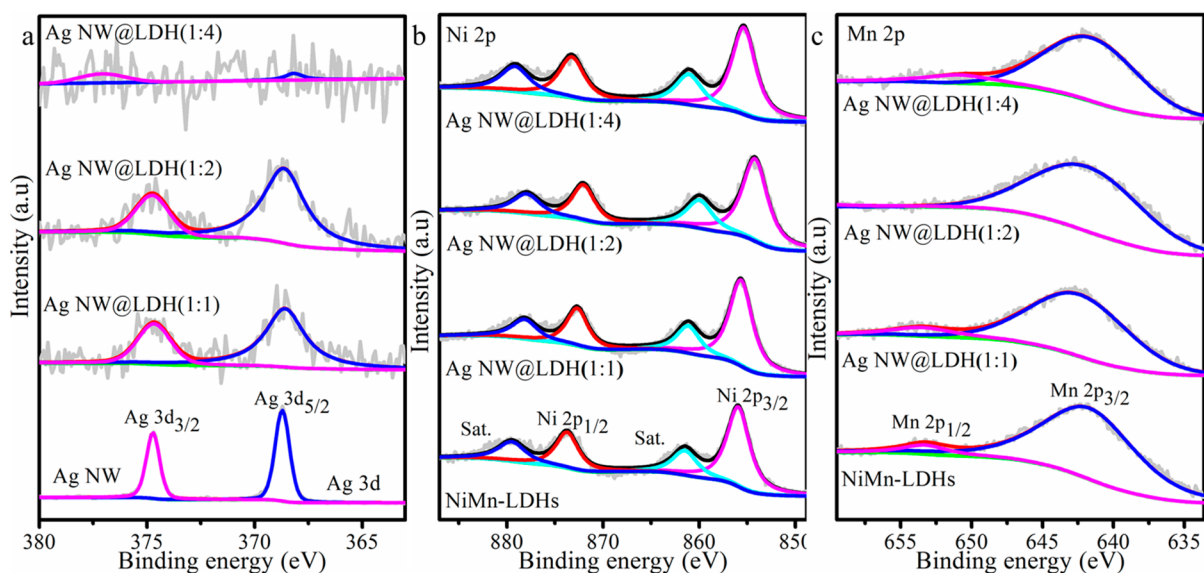
Figure 3. (a) XPS spectra of Ag 3d for bare Ag NWs and Ag NW@NiMn-LDH hybrids. (b) Ni 2p and (c) Mn 2p core levels for NiMn-LDHs and Ag NW@NiMn-LDH hybrids.
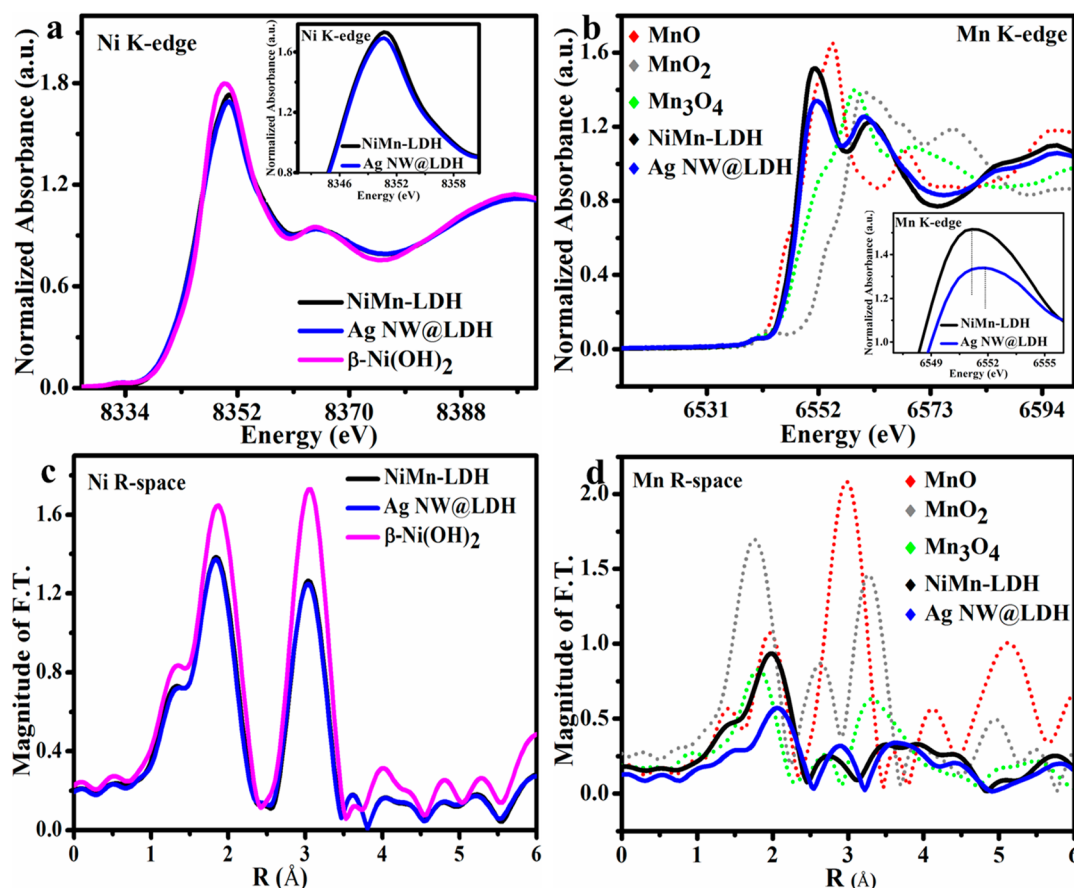

Figure 4. (a) Ni K-edge XANES spectra of the as-prepared NiMn-LDHs, Ag NW@NiMn-LDHs, and β-Ni(OH)$_2$. (b) Mn K-edge XANES spectra of NiMn-LDHs, Ag NW@NiMn-LDHs, and commercial MnO, MnO$_2$, and Mn$_3$O$_4$ for comparison. The insets in (a) and (b) show the enlarged Ni and Mn K-edge XANES. (c) Magnitude of FT-EXAFS spectra of the Ni K-edge. (d) Magnitude of FT-EXAFS spectra of the Mn K-edge.

between the interlayer galleries of NiMn-LDHs and the hybrid Ag NW@NiMn-LDHs. The Raman spectrum of NiMn-LDHs displays an intense peak at 553 cm^{-1} (Figure S7a). This band is attributed to the symmetric stretching vibration of MO

bonds. Upon the formation of the hierarchical 3D architectured Ag NW@NiMn-LDHs hybrid, three bands are observed in this region, at 464, 544, and 603 cm^{-1}. The underlying bands centered at 464 cm^{-1} and at ~544 cm^{-1} are attributed to

disordered or defected $Ni(OH)_2$. An intense peak detected at 603 cm^{-1} for Ag NW@NiMn-LDHs is attributed to the vibrational stretching mode of MnOOH.[25] The Raman shift at 3635 cm^{-1} is attributed to the −OH stretching of $Ni(OH)_2$ in the LDHs' surface (Figure S7b). This band can be also observed for Ag NW@NiMn-LDHs at 3650 cm^{-1}. This shift of −OH stretching to higher wavenumber for the Ag NW@ NiMn-LDHs hybrid is again due to the different structural environment. In the previous studies, bands in these positions were identified as the vibrational stretching mode of −OH groups.[26,27]

The wide-range survey X-ray photoelectron spectroscopy (XPS) spectrum of the as-prepared Ag NWs confirms the presence of Ag, C (for calibration), and O atoms (Figure S8). Ni, Mn, and O elements were detected in a wide-range survey of NiMn-LDHs. The overall survey XPS spectrum of the hierarchical 3D architectured Ag NW@NiMn-LDH hybrids (Figure S8) clearly confirms the existence of Mn, Ni, Ag, C (for calibration), and O elements. The XPS data of bare Ag NWs (Figure 3a) present two main peaks at 367.3 and 373.3 eV, corresponding to Ag 3d$_{5/2}$ and Ag 3d$_{3/2}$, respectively, indicating the typical peak of elemental Ag.[28] However, when it is core−shelled with NiMn-LDHs, the intensity of the Ag 3d peaks became very weak and broad along with a shift in peak position, confirming that the Ag NWs were well-confined within NiMn-LDHs shells. Further increasing the ratio of metal salts considerably diminished the intensity of the Ag 3d$_{5/2}$ and Ag 3d$_{3/2}$ peaks. In addition to the influence of dominant LDHs covered on the Ag surface, the electron escape depth in XPS is another cause for the weak signal because the technique has a limited penetration depth of several nanometers.[29] Thus, NiMn-LDHs dominates the surface and the binding energy shift might be due to the strong interaction of Ag cores and metal LDHs shells as a result of charge transfer. The Ni 2p spectrum of NiMn-LDHs (Figure 3b) shows two shakeup satellites and two main peaks found at 873.5 and 855.9 eV core levels, attributed to Ni 2p$_{1/2}$ and Ni 2p$_{3/2}$, respectively, indicating the existence of a high-spin Ni^{2+} oxidation state and about 0.3−0.7 eV higher than Ni 2p of Ag NW@NiMn-LDH hybrids. The binding energy of Mn 2p for NiMn-LDHs is 642.3 and 653.2 eV, analogous to Mn 2p$_{3/2}$ and Mn 2p$_{1/2}$, respectively, indicating the existence of Mn^{3+} and about 0.4 eV lower than the Ag NW@NiMn-LDH hybrids (Figure 3c). The O 1s spectrum of β-$Ni(OH)_2$ (Figure S9) displays three distinct peaks, whereas pristine NiMn-LDHs and the Ag NW@NiMn-LDHs hybrid show four oxygen contributions. The additional peak at 530.5 eV in both NiMn-LDHs and the Ag NW@NiMn-LDHs hybrid is related to the defected oxygen atoms.[30] Thus, the XPS analysis reveals that there is a firm interaction in the electronic structure between the Ag nanowire core and metal LDH shells in the hierarchical Ag NW@NiMn-LDHs hybrids. Accordingly, the hierarchical 3D architectured Ag NW@NiMn-LDHs hybrid exhibited better electron transfer when the ratio of Ag nanowires and NiMn-LDHs was 1:2, which is beneficial to promote the site activity of the catalyst. D. Zhou *et al.*[31] found that electron-rich metal sites (Ni or Fe) increase OER activity. Accordingly, as a result of the electron transfer effect of Ag cores with metal LDHs shells, the hierarchical 3D architectured Ag NW@NiMn-LDH hybrids can act as an efficient candidate for oxygen electrocatalysis.

X-ray absorption spectroscopy (XAS) was employed to investigate local structure atoms and the coordination nature of surface metals. The pre-edge peaks resulted from a 1s → 3d electric−quadrupole transition of around 8333.5 eV, and main absorption peaks at about 8350 eV due to the dipole electronic transition of 1s → 4p orbitals were obtained for the Ni K-edge (Figure 4a). The main absorption peak of the Ni K-edge for Ag NW@NiMn-LDHs slightly shifted to a lower position (inset in Figure 4a), suggesting the interaction between Ag NW cores and LDH shells. Figure 4b presents Mn K-edge XANES spectra of NiMn-LDHs, Ag NW@NiMn-LDHs, and commercial MnO, MnO$_2$, and Mn$_2$O$_3$ for comparison. XANES spectra of the Mn K-edge of the as-prepared Ag NW@NiMn-LDHs shifted to higher energy with reduced intensity when compared with the as-prepared NiMn-LDHs precursor, demonstrating a change in electronic structure and coordination numbers of the Mn species in Ag NW@NiMn-LDH hybrids.

Evidently, Mn K-edge XANES spectra display a weak pre-edge feature at around 6540.6 eV due to low-symmetry distortion of mixed allowed transitions through 4p → 3d, and an intense main edge feature at around 6551 eV arising from electric dipole transitions of 1s → 4p suggests the formal valence state of Mn^{3+} in NiMn-LDHs, consistent with XPS results and a previous report of Mn K-edge.[32,33] Although the energy of the pre-edge peak of the Mn K-edge of Ag NW@ NiMn-LDHs is nearly equivalent to NiMn-LDHs, the energy of the main-edge peak shifted to higher position (inset in Figure 4b) along with a sharp decrease in the intensity, attributed to the higher oxidation state of Mn and alteration of the electronic structure around the Mn atoms in Ag NW@ NiMn-LDHs. The corresponding Ni K-edge and Mn K-edge $k^2\chi(k)$ oscillation curves (Figure S10) of the NiMn-LDHs and Ag NW@NiMn-LDHs core−shell show a reduced amplitude of oscillation curves relative to β-$Ni(OH)_2$ for Ni K-edge and commercial MnO, MnO$_2$, and Mn$_2$O$_3$ for the Mn K-edge. These signalize the structural alteration in the coordination sphere of Ni and Mn atoms. The fitting analysis of the extended X-ray absorption fine structure (EXAFS) data is summarized in Figure 4c,d. As shown in Figure 4c, the peak at 1.80 Å in radial distribution function of the Ni K-edge is assigned to Ni−O coordination, and the peaks at around 3.00 Å are associated with Ni−M (M = Ni, Mn) coordination peaks. The decreased intensity of these coordination spheres relative to β-$Ni(OH)_2$ suggests a decrease in average coordination number (N) of Ni−O and Ni−M shells in both NiMn-LDHs and Ag NW@NiMn-LDHs along with the size reduction. Thus, compared to the average coordination number of Ni−O ($N = 6.00$) and Ni−Ni ($N = 6.00$) in β-$Ni(OH)_2$ (Table S2), the NiMn-LDHs exhibit a noticeable decrease in coordination number around the coordination sphere of Ni−M ($N = 5.77$), suggesting the presence of coordinatively unsaturated Ni sites. Similarly, the average coordination numbers of Ni−O ($N = 5.78$) and Ni−M ($N = 5.69$) coordination spheres also decrease in hierarchical 3D architectured Ag NW@NiMn-LDH hybrids. This information describes the presence of oxygen vacancies and coordinatively unsaturated Ni sites in both NiMn-LDHs and Ag NW@NiMn-LDH hybrids. Furthermore, the intensity of Mn−O coordination spheres of Ag NW@NiMn-LDHs is significantly reduced relative to the pristine NiMn-LDHs (Figure 4d and Table S3), suggesting that further increased coordinatively unsaturated Mn sites and Mn atoms exposed on the surface of NiMn-LDHs are partially saturated with O atoms. In fact, coordinatively unsaturated metal atoms cause structural distortion and defects that can tune the electronic properties
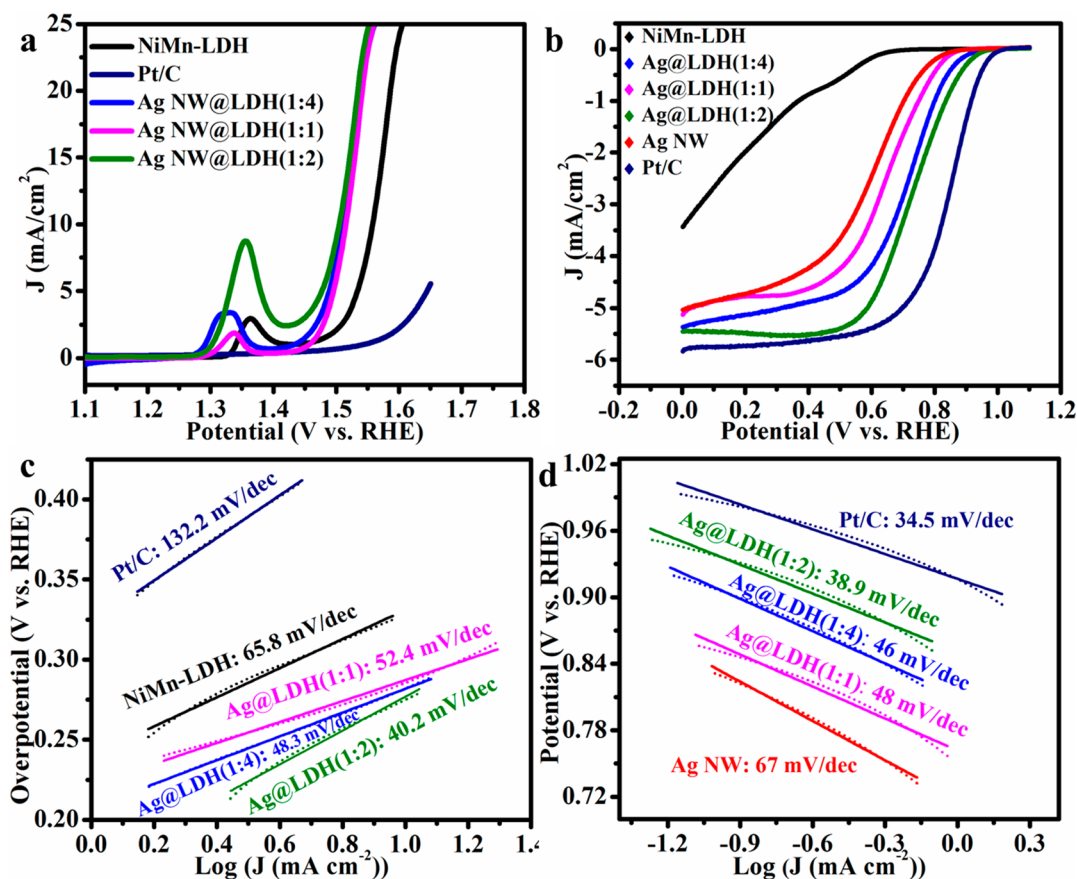
Figure 5. (a) OER LSV curves of NiMn-LDHs, hierarchical Ag NW@NiMn-LDH hybrids of different ratios of metal salts and Ag NWs, and commercial Pt/C at a rotation rate of 1600 rpm. (b) ORR LSV curves of Ag NWs, NiMn-LDHs, hierarchical Ag NW@NiMn-LDH hybrids, and commercial Pt/C in O_2-saturated 1 M KOH at 1 mV/s sweep rate and 1600 rpm rotation rate. (c) OER and (d) ORR Tafel slopes for each sample.

and enhance the site activity of the catalyst. Therefore, the presence of coordinatively unsaturated metal sites causes vacancy defects and engineer disorder that could greatly affect the electronic structure of the hierarchical 3D architectured Ag NW@NiMn-LDH hybrids, which in turn plays a significant role in tuning the catalytic properties of the active sites and hence attaining improved catalytic activities.

The electrocatalytic properties of the hierarchical 3D architectured Ag NW@NiMn-LDH hybrids along with the pristine NiMn-LDHs and commercial IrO_2 and Pt/C with respect to OER were first assessed using the usual three-electrode method in 1 M KOH aqueous solution (70 μg cm^{-2} catalyst loading was used for all samples). The polarization curves in Figure 5a and Figure S11 show that the hierarchical 3D architectured Ag NW@NiMn-LDH hybrids exhibit a much higher OER activity with a lower onset potential than the pristine NiMn-LDHs and commercial IrO_2 and Pt/C. This could be due to the strong coupling effect between the Ag NW core and LDH shells and exposed accessible coordinatively unsaturated Ni and Mn sites. Furthermore, the more accessible Ni sites resulting from the hierarchical open-channel structure of the LDH shells in the 3D architectured Ag NW@NiMn-LDHs boosted the OER activity, as evidenced by a higher $Ni^{2+/3+}$ redox peak area. Moreover, the intimate connection between Ag NW cores and NiMn-LDH shells could enable electron transfer and induce a strong synergistic effect for the OER. To further reveal the effect of LDH shells grown on the conductive Ag NW cores, a series of electrochemical

measurements were carried out on Ag NW@NiMn-LDHs core−shell nanosheets with various LDH ratios (from 1:1 to 1:4), while keeping the amount of Ag NWs constant. As shown in Figure 5a and Figure S11, the OER onset overpotentials of Ag NW@NiMn-LDHs(1:2), Ag NW@NiMn-LDHs(1:4), Ag NW@NiMn-LDHs(1:1), NiMn-LDHs, and commercial IrO_2 and Pt/C were 0.19, 0.20, 0.22, 0.25, 0.26, and 0.29 V *versus* RHE, respectively. The hierarchical 3D architectured Ag NW@NiMn-LDHs(1:2) core−shell nanosheets show a pronounced OER catalytic activity with an earliest onset overpotential of 0.19 V. Specifically, the hierarchical 3D architectured Ag NW@NiMn-LDHs(1:2) core−shell electrode yields current densities of 10 and 25 mA cm^{-2} at an applied overpotential of 270 and 320 mV, respectively. In contrast, the prominent ORR electrocatalyst Pt/C exhibits very poor OER performance without reaching 10 mA cm^{-2} up to 1.665 V. Thus, our hierarchical 3D architectured Ag NW@NiMn-LDHs(1:2) hybrid stands out as vastly an active electrocatalyst for OER.

In addition, the OER activity of the hybrid catalysts and pristine NiMn-LDHs was evaluated by scanning from high to low potentials at a scan rate of 1 mV/s as shown in Figure S12. Similar to the OER polarization curves obtained from low to high potentials, the OER activity of the hierarchical 3D nanostructure of the Ag NW@NiMn-LDHs(1:2) hybrid is better than its counterparts. The cathodic waves found between ∼1.2 and 1.3 V are attributed to the transformation of the Ni^{3+} to Ni^{2+} redox couple under this condition. The
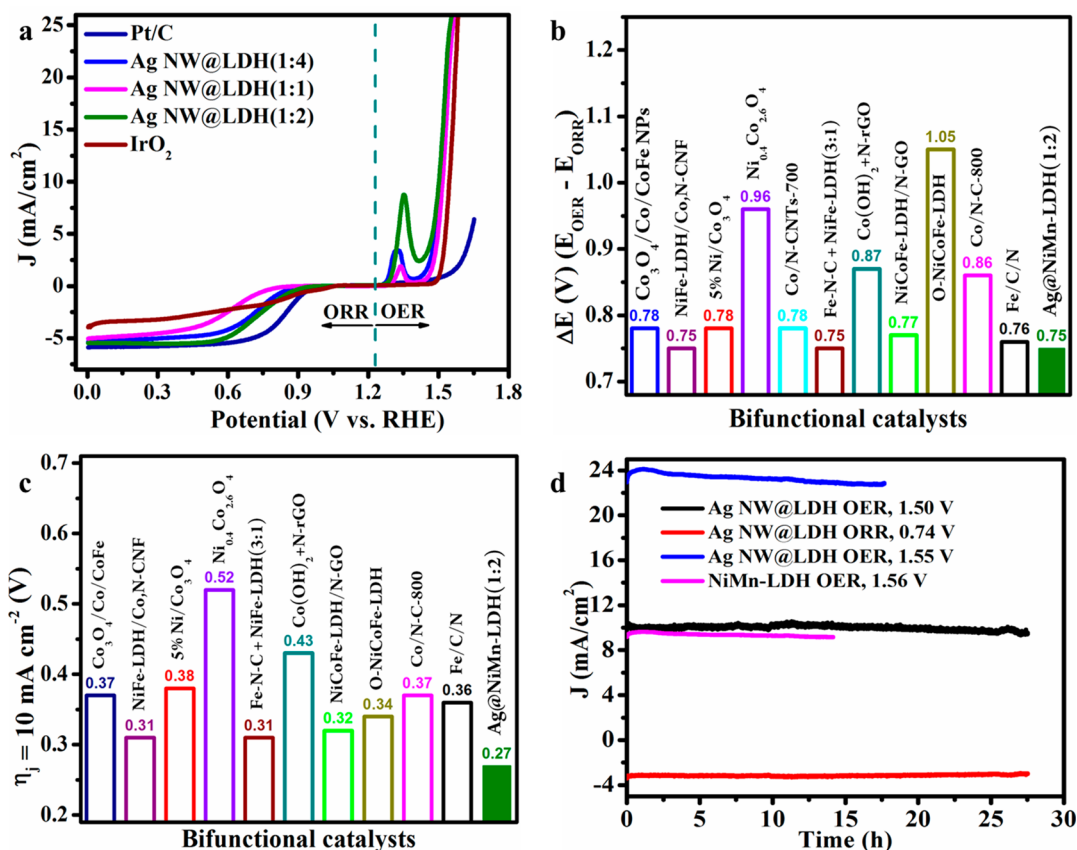
Figure 6. (a) OER/ORR overall bifunctional activities of the hierarchical 3D architectured Ag NW@NiMn-LDH hybrids and commercial IrO$_2$ and Pt/C catalysts. (b) Comparison of the potential difference (ΔE) between OER at j = 10 mA/cm^2 and ORR at j = −3 mA/cm^2 and (c) the OER overpotential required to deliver a current density of 10 mA cm^{-2} for the hierarchical Ag NW@NiMn-LDHs(1:2) hybrid with other electrocatalysts in published literature. (d) Current−time chronoamperometric responses of NiMn-LDHs (at a fixed potential of corresponding current densities of 10 mA cm^{-2}) and Ag NW@NiMn-LDHs(1:2) electrodes carried out under constant potential of corresponding current densities of 10 and 25 mA cm^{-2} (OER) and −3 mA cm^{-2} (ORR) in 1 M KOH solution.

distinct anodic and cathodic peaks could be due to the site activity and site population differences of the hybrid catalysts resulting from the electronic/structural differences of the Ni sites.

The electrochemical ORR activity of the as-prepared samples was assessed in 1 M KOH aqueous solution using a three-electrode system. The relative cyclic voltammetry (CV) of both O$_2$- and Ar-saturated 1 M KOH electrolyte at a scan rate of 50 mV s^{-1} was recorded as shown in Figure S13. The Ag NW@NiMn-LDHs core−shell exhibited a featureless CV curve in Ar-saturated aqueous solution, whereas a noticeable cathodic peak appeared at about +0.95 V after being saturated with O$_2$ gas, signifying tremendous ORR activity. To compare and further scrutinize the roles of Ag NW and LDH composition on ORR activity, the LSVs of NiMn-LDHs, Ag NWs, Ag NW@NiMn-LDHs(1:1), Ag NW@NiMn-LDHs(1:4), Ag NW@NiMn-LDHs(1:2), and Pt/C were executed as shown in Figure 5b. Accordingly, the ORR activity of the hierarchical Ag NW@NiMn-LDHs(1:2) core−shell is superior relative to the counterparts. The half-wave potential and onset potential of Ag NW@NiMn-LDHs(1:2) were 0.75 and 0.96 V, respectively, which are closer to the Pt/C catalyst (0.83 and 0.98 V) and essentially more positive than Ag NW@NiMn-LDHs(1:4) (0.70 and 0.93 V), Ag NW@NiMn-LDHs(1:1) (0.62 and 0.87 V), and Ag NWs (0.56 and 0.85 V). This result suggests that coating the surface of conductive Ag NWs cores with NiMn-LDHs shells at an appropriate level

can efficiently enhance electrochemical activity. An excess of LDHs leads to a decrease of the electrocatalytic activity, which might be a result of the dense packing of LDHs on the conductive Ag NWs, which hinders charge transfer and reduces accessible site populations. Similarly, the hybrid Ag NW@NiMn-LDHs(1:1) shows low ORR activity as compared to Ag NW@NiMn-LDHs(1:2). These suggest that the LDH shells have a detrimental effect on ORR activity, and when it is not entirely embedded on Ag nanowires, the OH adsorption easily accesses the inner Ag sites, which in turn reduces the accessible site populations. Thus, the higher ORR activity of the hierarchical 3D architectured Ag NW@NiMn-LDHs(1:2) hybrid is likely due to the synergetic effect between the optimal ratio of Ag and metal LDHs.

To further investigate the electrochemical kinetics and number of transferring electrons (n), the rotating disk electrode (RDE) measurements were implemented at different rotation speeds (100−2500 rpm) during the ORR process. Accordingly, the polarization curves and the corresponding Koutecky−Levich plots are shown in Figure S14. Based on the slopes of K−L plots, n was estimated to be 3.95 for the hybrid Ag NW@NiMn-LDHs(1:2), higher than that of Ag NW@NiMn-LDHs(1:4) (n = 3.81) and Ag NW@NiMn-LDHs(1:1) (n = 3.52) at a voltage range of 0.70−0.45 V. The variation in the number of electron transfers suggested that the hierarchical 3D architectured Ag NW@NiMn-LDHs(1:2) is substantially more electro-active and selective than its counterparts and

exhibits almost the same features as the ORR benchmark catalyst. These results suggest that there is an optimal ratio between NiMn-LDHs and Ag nanowires for the best catalytic performance.

Furthermore, the ORR/OER Tafel slopes of each sample are displayed in Figure 5c,d. The OER Tafel slopes of Ag NW@NiMn-LDHs(1:2), Ag NW@NiMn-LDHs(1:4), Ag NW@NiMn-LDHs(1:1), NiMn-LDHs, and Pt/C were 40.2, 48.3, 52.4, 65.8, and 132.2 mV dec^{-1}, respectively, whereas the ORR Tafel slopes were 34.5, 38.9, 46, 48, and 67 mV dec^{-1} for Pt/C, Ag NW@NiMn-LDHs(1:2), Ag NW@NiMn-LDHs(1:4), Ag NW@NiMn-LDHs(1:1), and Ag NWs, respectively. Evidently, the OER/ORR Tafel slope of Ag NW@NiMn-LDHs(1:2) is much lower than the counterparts. Thus, the lower Tafel slope of the hierarchical 3D architectured Ag NW@NiMn-LDHs(1:2) hybrid implies more favorable ORR/OER kinetics.

We further note the performances of Ag NW@NiMn-LDHs(1:2) as a bifunctional electrocatalyst, as illustrated in Figure 6a. For comparison, Ag NW@NiMn-LDHs(1:4), Ag NW@NiMn-LDH(1:1), and commercial IrO$_2$ and Pt/C were used as the counterparts in a 1 M KOH aqueous solution. Although the ORR activity of Ag NW@NiMn-LDHs(1:2) is inferior to the commercial Pt/C, the comparatively low onset overpotential indicated that the coupling effect between Ag NWs and LDHs enhanced the site activity of the catalyst toward ORR. Furthermore, Ag NW@NiMn-LDHs(1:2) has an outstanding potential difference (ΔE) between the OER overpotential at the current density of 10 mA cm^{-2} and the ORR half-wave overpotential at the current density of -3 mA cm^{-2} when compared with the reported literature so far (Figure 6b). While in 2015 a Ni-based trinary LDH electrocatalyst exhibited a potential difference of 1.05 V,[34] our hierarchical 3D Ag NW@NiMn-LDHs(1:2) core−shell architecture reached a value of 0.75 V and thus signifies the most efficient OER/ORR bifunctional oxygen electrocatalyst reported to date (Table S6). The OER overpotentials at the current density of 10 mA cm^{-2} of our hierarchical Ag NW@NiMn-LDHs core−shell architecture and certain previously reported literature are also compared, as shown in Figure 6c. Accordingly, the Ag NW@NiMn-LDHs(1:2) hybrid exhibited the lowest OER overpotential at the current density of 10 mA cm^{-2}, further revealing superior OER activity. These results suggest that the hierarchical 3D architectured Ag NW@NiMn-LDHs could serve as an efficient and nonprecious metal bifunctional electrocatalyst toward OER/ORR. Such highly active OER/ORR activities of the hierarchical 3D architectured Ag NW@NiMn-LDHs is essentially due to the supported conductive Ag NWs, since NiMn-LDHs itself had poor conductivity and a sluggish OER activity, with a Tafel slope of 65.8 mV dec^{-1} and high onset overpotential of 250 mV. Nevertheless, Ag NWs played a key role in improving both the OER and ORR activity of Ag NW@NiMn-LDHs relative to unsupported NiMn-LDHs. First, Ag NWs imparted high conductivity to the Ag NW@NiMn-LDH hybrids. According to electrochemical impedance spectroscopy (Figure S15) and 4-point probe (Table S4) results, the pristine NiMn-LDHs suffered from low conductivity. The smaller semicircle evidenced in the Nyquist plot for Ag NW@NiMn-LDHs confirmed its reduced resistance compared to the pristine NiMn-LDHs (i.e., improved conductivity), thus benefiting the dispersion of LDH nanosheets and electron transfer.

To understand the reason behind the superb bifunctional activity of Ag NW@NiMn-LDHs toward ORR and OER

activities, the electrochemically active surface areas (ECSAs) of Ag NW@NiMn-LDHs(1:2), Ag NW@NiMn-LDHs(1:4), and NiMn-LDHs were acquired from CV curves in 1 M KOH electrolyte (Figure S16). By plotting the current density at 0.71 V versus RHE against the scan rate, the double-layer capacitance (C_{dl}) equivalent to half of the average absolute value of the linear slope was obtained and is usually denoted as the ECSA.[35−38] The calculated C_{dl}, which represents the ECSA, as illustrated in Figure S16, of Ag NW@NiMn-LDHs(1:2) had an ECSA two times larger than that of Ag NW@NiMn-LDHs(1:4) and about six times larger than that of the pristine NiMn-LDHs. The substantial enhancement in ECSA value of the 3D architectured Ag NW@NiMn-LDHs can be ascribed to the open-channel hierarchical structure of NiMn-LDHs shells on the surface of Ag NWs cores. Besides improving the conductivity of the hybrids, the presence of Ag NWs also enhances the dispersion and prevents structural restacking of the LDHs, and a few layers of LDHs shells jointly offers a large ECSA. Thus, the higher effective ECSA or accessible site populations of the hierarchical Ag NW@NiMn-LDHs(1:2) at the same catalyst loading contributed to the higher activity relative to Ag NW@NiMn-LDHs(1:4) and the pristine LDHs.

The durability of the electrocatalytic electrode is another key and serious matter when considering the catalyst for applications. As displayed in Figure 6d, the Ag NW@NiMn-LDHs(1:2) hybrid showed excellent durability for 27.5 h at an overpotential of 270 mV, corresponding to 10 mA cm^{-2} for OER and 480 mV for ORR. Simultaneously, the hierarchical 3D architectured Ag NW@NiMn-LDHs(1:2) hybrid exhibits excellent durability (6% activity decay after 17 h) at an overpotential corresponding to the current density of 25 mA cm^{-2}, suggesting the Ag NW@NiMn-LDH hybrid has excellent stability for water oxidation. The durability test was also conducted for pristine NiMn-LDHs at an overpotential of 330 mV, and the material lost 15% of its activity after 14 h. The quick deterioration in current density is essentially due to blockage of several active sites of the catalyst by the accumulation of evolved O$_2$ bubbles. Furthermore, the hybrid Ag NW@NiMn-LDHs(1:2) exhibited excellent cyclic stability up to 4000 cycles in 1 M KOH at a scan rate of 50 mV/s (Figure S17). It was noticeable that the tight interaction and the electronic effect between the hierarchical 3D structure of LDH shells and conductive Ag NW cores stabilize the structure. Furthermore, the exposure of more accessible active sites results from the hierarchical 3D open-pore structure of LDHs, and the presence of Ag NWs helps to prevent the structural restacking of LDH nanosheets, which makes the structure of the hybrid more stable. To rationalize the structural stability of the hierarchical 3D architectured Ag NW@NiMn-LDHs(1:2) catalyst after a long-term stability test during the OER and ORR, XPS spectra were acquired and are shown in Figure S18. The XPS spectra reveal that Ag 3d, Ni 2p, and Mn 2p peaks shifted to higher binding energy after a long-term stability test, indicating the presence of a high valence state. This result means that all the electronic states of Ni, Mn, and Ag sites in the Ag NW@NiMn-LDHs(1:2) hybrid have been changed greatly after the long-term stability test. Therefore, the XPS data show that Ni, Mn, and Ag sites were involved in the electrochemical reactions, which will be beneficial for the synergetic effect and would be responsible for the excellent bifunctional performance of the Ag NW@NiMn-LDHs hybrid. Moreover, the morphology and crystal-

Scheme 1. Schematic illustration of hierarchical 3D architectured Ag NW@NiMn-LDH hybrids.
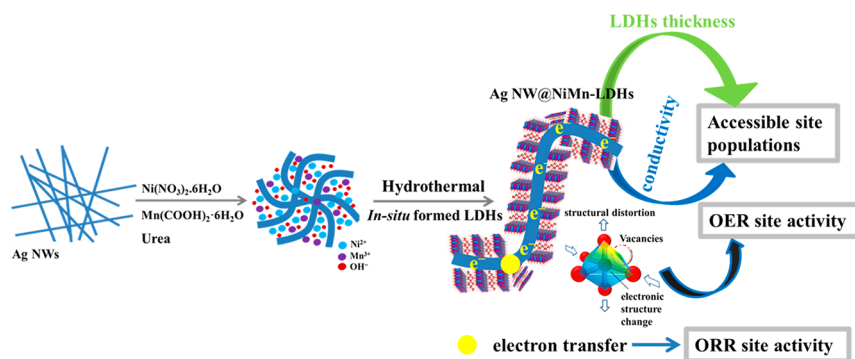
linity of the hierarchical 3D nanostructure of the Ag NW@ NiMn-LDHs(1:2) hybrid were evaluated after a 12 h stability test during the OER using TEM and HR-TEM. As shown in Figure S19a−c, the morphology and crystallinity of the Ag NW@NiMn-LDHs core−shell are well preserved. The EDS mapping images (Figure S19d,e) identified the typical core− shell nanostructure of the Ag NW@NiMn-LDHs hybrid, which clearly shows that Ni and Mn atoms are homogeneously distributed on the surface of the Ag nanowires. The electron diffraction patterns (Figure S19f) show the same situation after the stability test as the initial state. Thus, the TEM and HR-TEM images of the hybrid catalyst reveal that there is no structural and phase change after a long-time stability test, and the hierarchical 3D nanostructure of Ag NW@NiMn-LDHs core−shell is well maintained.

To get some deep insight into the effect of defects on catalytic performance, density of states (DOS) were computed by density functional theory (DFT) calculations. The model of NiMn-LDHs is illustrated in Figure S20a, where the atomic ratio of Ni/Mn is 3:1 and CO_3^{2-} is the intercalated anion. As shown in Figure S20b, the defect-free NiMn-LDHs is semiconducting with a noticeable band gap near the Fermi level in both spin-up and spin-down states, while the oxidation states of Ni and Mn can be confirmed as 2+ ($3d^8$) and 3+ ($3d^4$), respectively, according to their electron configuration. As shown in Figure S20c,d and Figure S21a−d, the DOS were also computed for defected NiMn-LDHs with the oxygen vacancies near Ni and Mn sites. As a result, the integral partial DOS (PDOS) of Ni-3d and Mn-3d were estimated for defect-free and defected NiMn-LDHs (Table S5). Accordingly, when the oxygen vacancy was created on the Mn site, the resultant densities of electrons for occupied states in Ni and Mn sites are 0.08 and 0.19 e$^-$/atom, respectively. However, when the oxygen vacancy is created on the Ni site, the resultant densities of electrons for occupied states in Ni and Mn sites are 0.59 and −0.08 e$^-$/atom, respectively. The integrated PDOS clearly shows that when an oxygen vacancy is created on the Mn site, the electron density for an occupied state of the Mn site is more positive relative to the Ni sites, suggesting that the deficiency of electron density surrounding the Mn site is more favorable. The calculations properly explain the electronic properties in the XPS results, and the defect surrounding the Mn site in NiMn-LDHs is also consistent with the XAS results. As a result, the hybridization of defective Ni-3d and Mn-3d with 2p states of O would result in a much stronger O adsorption, which intrinsically enhances the OER activity of NiMn-LDHs. On the other hand, the presence of defects lowers the band gap and improves the electric conductivity of

NiMn-LDHs, which is promising for high-performance electrocatalysts.

The hierarchical 3D architectured Ag NW@NiMn-LDH hybrids are representatively used as an efficient bifunctional electrocatalyst toward the OER and ORR. The significantly enriched bifunctional performance of Ag NW@NiMn-LDHs(1:2) is attributed to its optimal structural characteristics for electrocatalysis including less dense packing of NiMn-LDHs nanosheets, highly exposed coordinatively unsaturated metal active sites, improved electrical conductivity, and a combination of a hierarchical 3D open-pore nanostructure of the LDHs shells. As shown in Scheme 1, incorporating Mn into close-packed β-Ni(OH)$_2$ produces NiMn-LDHs with the expanded space of intersheet layers having coordinatively unsaturated metal sites. The introduction of conductive Ag NWs into NiMn-LDHs generates the hierarchical 3D structure of architectured Ag NW@NiMn-LDH hybrids with an open-pore structure of the LDHs shells and possessing more coordinatively unsaturated metal sites. Moreover, the intro-duction of conductive Ag NWs into NiMn-LDHs increases conductivity of the hybrids and decreases the structural restacking of NiMn-LDHs shells, offering a large ECSA relevant to the site populations.

The advantage of core@shell hierarchical nanostructures is the interconnecting non-noble conductive core, which further alters the electronic structure of LDH shells and efficient transportation of electrons from highly conductive Ag NW cores to the enclosed 3D hierarchical NiMn-LDH shells. Thus, the electronic effect between Ag NW core and metals in an LDH shell has tuned the site activity and synergistically promoted the ORR/OER activity. The superb OER activity of the hierarchical 3D architectured Ag NW@NiMn-LDH hybrids resulted from the synergistically hierarchical 3D open-pore structure of the LDH shells, conductivity improve-ment, and small thickness of LDH shells jointly associated with the OER site populations.

Moreover, the synergies of coordinatively unsaturated metal sites and the oxygen vacancies originated from the hierarchical structure of the vertical growth of LDHs on Ag NW cores cause more accessible distorted and defected sites that jointly contribute to active OER site activity, thereby enhancing the catalytic activity of the Ag NW@NiMn-LDH hybrids toward the OER. While pristine LDHs and Ag NWs were incapable of possessing such outstanding features, their catalytic activities were far from satisfactory. Thus, by combining the Tafel slope, onset potentials of all samples in OER/ORR processes, and the ECSA, we realistically drew the conclusion that the hierarchical 3D architectured Ag NW@NiMn-LDH hybrids are an efficient
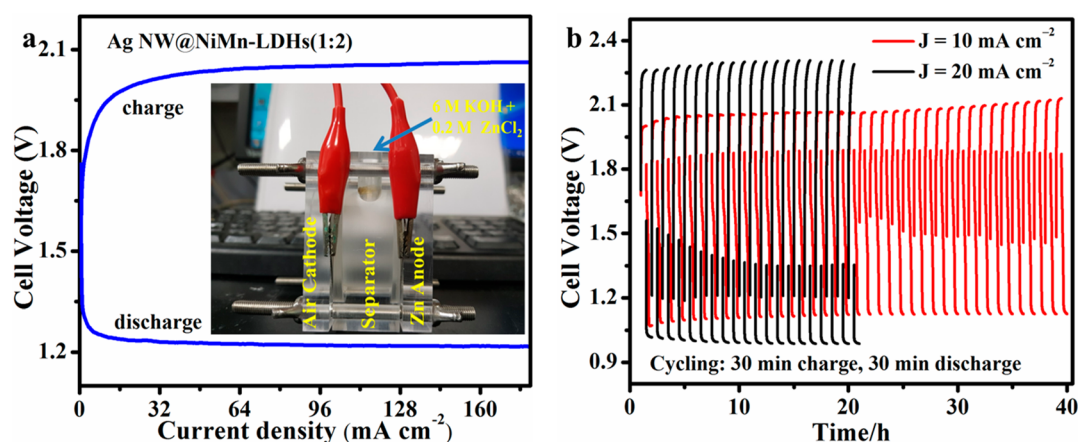
Figure 7. (a) Charge−discharge polarization curves. The inset in (a) shows a digital image of our home-built Zn−air battery cell. (b) Long-time cycling performances of a Zn−air battery with the Ag NW@NiMn-LDHs(1:2) air electrode at 10 mA cm^{-2} with a 40 h cycle period and 20 mA cm^{-2} (20 h cycle period).

electrocatalyst for the bifunctional ORR/OER activity. Therefore, the hierarchical 3D architectured Ag NW@NiMn-LDH hybrids possess superior bifunctional OER/ORR activity as well as great durability, endowing them with a promising bifunctional electrocatalyst activity for future applications.

To further demonstrate the bifunctional activity of the hierarchical 3D architectured Ag NW@NiMn-LDH(1:2) hybrids, the home-built rechargeable Zn−air battery was used to evaluate their practical applications. The inset in Figure 7a shows a digital image of our home-built Zn−air battery cell. Figure 7a indicates the charge and discharge polarization curves of a rechargeable Zn−air battery using a Ag NW@NiMn-LDHs(1:2) electrode loaded on carbon fiber paper. The battery exhibited a charge−discharge voltage gap of ∼0.77 V at 10 mA cm^{-2}, smaller than the reported literature,[39,40] demonstrating better rechargeability of the hierarchical 3D architecture of the Ag NW@NiMn-LDHs(1:2) hybrid. Essentially, when repeatedly charged or discharged for a total of 40 h with a 1 h per cycle period, at 10 mA cm^{-2}, the battery showed high cycling stability (Figure 7b). Furthermore, the long-time cycling performances of charge and discharge were also performed at 20 mA cm^{-2} for an additional 20 h with a 1 h per cycle period. Although the voltage change can be differentiated on both the charge and discharge segments, the catalyst and cell still exhibited no obvious degradation for 20 h.

CONCLUSION

In summary, 3D architectured Ag NW@NiMn-LDH hybrids have been developed as an efficient bifunctional oxygen electrocatalyst, consisting of highly conductive silver nanowires in the core decorated with hierarchical NiMn-LDHs as the shell. Both the OER and the ORR activities of the hierarchical 3D architectured Ag NW@NiMn-LDHs can be modified by varying the LDH shells. The preeminent bifunctional activity and durability of the nanostructured oxygen electrocatalysts for the reversible ORR/OER in basic electrolyte were achieved by hierarchical Ag NW and NiMn-LDH nanosheets (1:2), when compared to the state-of-the-art Pt/C and IrO$_2$. Thus, the strong coupling effect between the hierarchical 3D open-pore structure of LDHs and Ag NWs, a few layers of LDHs shells, and improved conductivity are mutually associated with the accessible site populations and synergistically enhanced the

ORR/OER activities of Ag NW@NiMn-LDHs. Furthermore, the coordinatively unsaturated active metal centers exposed on the surface causes defects of active metal centers and engineering structural distortion relevant to the site activity, which in turn dictates active sites for the improved OER/ORR bifunctional activities. The coupled electronic interaction and structural disorder further change the intrinsic catalytic activity of individual active site. Thus, the resultant synergies between conductive Ag NW cores and the hierarchical 3D open-pore structure of LDHs shells of Ag NW@NiMn-LDHs boosted the bifunctional ORR/OER activities and durability. Therefore, the proposed strategy of a core−shell hierarchical 3D architecture of LDHs with a conductive nanomaterial proves to be effective in creating highly active, resourceful, and durable heterogeneous catalysts.

EXPERIMENTAL PART

Synthesis of 2D NiMn-LDHs Nanosheet Precursor Phase. In a typical preparation, Ni(NO$_3$)$_2$·6H$_2$O and Mn(COOH)$_2$.6H$_2$O with a Ni/Mn molar ratios equal to 3 are dissolved in 20 mL of DI water to achieve a total molarity of 40 mM and vigorously stirred for 10 min to make a homogeneous solution. Then urea (4 mmol) was subsequently introduced into the above solution under stirring to favor the precipitation. The resulting solutions were treated hydrothermally at 120 °C for 12 h in a Teflon-line stainless-steel autoclave. After naturally cooling to ambient temperature, the product was collected by centrifuge, washed several times with ethanol and deionized water, and then freeze-dried overnight.

Synthesis of Hierarchical 3D Architectured Silver Nano-wire@NiMn Layered Double Hydroxide Hybrids. Silver nano-wires were synthesized using simple procedures previously described in the literature[41] with simple modification. Ag NW@NiMn-LDHs was prepared *via* hydrothermal methods.[42] In a typical synthesis, the as-prepared Ag NWs were dispersed into 40 mL of DI water ultrasonically (0.04 mol L^{-1}). A 0.6 mmol amount of Ni(NO$_3$)$_2$·6H$_2$O and 0.2 mmol of Mn(COOH)$_2$.6H$_2$O were dissolved into 40 mL of a Ag NW suspension. Afterward, 4 mmol of urea was added into the mixture under continuous stirring, and the resulting mixed suspensions were treated hydrothermally in a Teflon-line stainless-steel autoclave at 120 °C for 18 h. After being naturally cooled to room temperature, the product was obtained by centrifugation, washed with deionized water and ethanol, and subsequently freeze-dried. The molar ratios of Ag NWs to metal salts were varied from 1:1 to 1:4.

Material Characterization. Morphologies and elemental analysis of the as-synthesized materials were investigated by an SEM (JSM

6500F, JEOL) assimilated with EDX. X-ray diffraction patterns were collected on an XRD-300W with Cu Kα radiation under the operation conditions of 30 kV, λ = 1.54 Å, and 10 mA. The intercalated anions were analyzed using Fourier transform infrared (FT-IR) spectrophotometry (FTS-3500, Bio-Rad, USA). Raman spectra were obtained using a confocal Raman microscope (Protrustech Co., Ltd.) with a laser source of 633 nm and power of 1−3 mW. Surface composition and oxidation states were collected from XPS (PHI, 1600S) at the beamline station 24A at the National Synchrotron Radiation Research Center (NSRRC) in Hsinchu, Taiwan. XAS data of the as-prepared materials were recorded at the beamline station BL01C1 and BL17C1 in NSRRC Hsinchu, Taiwan.

Electrochemical Measurements. The electrocatalytic performances were done using a potentiostat (PGSTAT302N, Metrohm Autolab) workstation integrated with a rotational system (Pine Research Instrumentation, Durham, NC, USA) with a standard three-electrode cell in 1 M KOH solution. A graphite rod, a modified glassy carbon electrode (GCE), and Ag/AgCl/saturated KCl were used as the counter, working, and reference electrodes, respectively. The working electrode was prepared by dispersing 5 mg of the catalysts in 1 mL of isopropanol and deionized water (3:1) and 70 μL of Nafion solution (0.05 wt % in alcohol) for 30 min using ultrasonication to homogenize the catalyst ink. Subsequently, 14 μL (loading = 70 μg cm^{-2}) of catalyst ink was casted on a GCE (0.197 cm^2 in area).

Zn−Air Battery Test. To further demonstrate the bifunctional activity of the hierarchical 3D architectured Ag NW@NiMn-LDHs hybrid, a home-built rechargeable Zn−air battery was used. The as-prepared catalyst was loaded on carbon cloth (1 cm × 1 cm) as the air cathode with the catalyst loading of 4.6 mg cm^{-2} and paired with a Zn foil (2 cm × 2 cm) anode. The electrolyte solution used was 6 M KOH with 0.2 M zinc chloride (about 25 mL). A potentiostat (PGSTAT302N, Metrohm Autolab) workstation was used to test the Zn−air battery.

ASSOCIATED CONTENT

Ⓢ Supporting Information

The Supporting Information is available free of charge at https://pubs.acs.org/doi/10.1021/acsnano.9b07487.

Additional SEM images, TEM (before and after long-time stability test), HR-TEM (before and after long-time stability test), EDX, XRD, FT-IR, BET, Raman spectra, XPS (before and after long-time stability test), XANES and EXAFS analysis, electrochemical results (CV, LSV, ECSA, and durability), conductivity result measured by 4-pont probe, EIS, computational DFT calculations, and performance comparison table (PDF)

AUTHOR INFORMATION

Corresponding Authors

Meng-Che Tsai − NanoElectrochemistry Laboratory, Graduate Institute of Applied Science and Technology and Sustainable Energy Development Center, National Taiwan University of Science and Technology, Taipei 106, Taiwan; Email: mctsai@mail.ntust.edu.tw

Wei-Nien Su − NanoElectrochemistry Laboratory, Graduate Institute of Applied Science and Technology and Sustainable Energy Development Center, National Taiwan University of Science and Technology, Taipei 106, Taiwan; ⓘ orcid.org/0000-0003-1494-2675; Email: wsu@mail.ntust.edu.tw

Hongjie Dai − Department of Chemistry, Stanford University, Stanford, California 94305, United States; ⓘ orcid.org/0000-0002-4906-4502; Email: hdai1@stanford.edu

Bing-Joe Hwang − NanoElectrochemistry Laboratory, Department of Chemical Engineering, NanoElectrochemistry Laboratory, Graduate Institute of Applied Science and Technology, and Sustainable Energy Development Center, National Taiwan University of Science and Technology, Taipei 106, Taiwan; National Synchrotron Radiation Research Center, Hsin-Chu 30076, Taiwan; ⓘ orcid.org/0000-0002-3873-2149; Email: bjh@mail.ntust.edu.tw

Authors

Soressa Abera Chala − NanoElectrochemistry Laboratory, Department of Chemical Engineering and Sustainable Energy Development Center, National Taiwan University of Science and Technology, Taipei 106, Taiwan

Kassa Belay Ibrahim − NanoElectrochemistry Laboratory, Graduate Institute of Applied Science and Technology, National Taiwan University of Science and Technology, Taipei 106, Taiwan

Balamurugan Thirumalraj − NanoElectrochemistry Laboratory, Department of Chemical Engineering and Sustainable Energy Development Center, National Taiwan University of Science and Technology, Taipei 106, Taiwan; ⓘ orcid.org/0000-0001-9369-1901

Ting-Shan Chan − National Synchrotron Radiation Research Center, Hsin-Chu 30076, Taiwan

Jyh-Fu Lee − National Synchrotron Radiation Research Center, Hsin-Chu 30076, Taiwan

Complete contact information is available at:
https://pubs.acs.org/10.1021/acsnano.9b07487

Notes

The authors declare no competing financial interest.

REFERENCES

(1) Raj, C. R.; Samanta, A.; Noh, S. H.; Mondal, S.; Okajima, T.; Ohsaka, T. Emerging New Generation Electrocatalysts for the Oxygen Reduction Reaction. *J. Mater. Chem. A* **2016**, *4*, 11156−11178.

(2) Wang, H.-F.; Tang, C.; Zhu, X.; Zhang, Q. A 'Point-Line-Point' Hybrid Electrocatalyst for Bi-Functional Catalysis of Oxygen Evolution and Reduction Reactions. *J. Mater. Chem. A* **2016**, *4*, 3379−3385.

(3) Yang, J.; Zhu, G.; Liu, Y.; Xia, J.; Ji, Z.; Shen, X.; Wu, S. Fe$_3$O$_4$-Decorated Co$_9$S$_8$ Nanoparticles *In Situ* Grown on Reduced Graphene Oxide: A New and Efficient Electrocatalyst for Oxygen Evolution Reaction. *Adv. Funct. Mater.* **2016**, *26*, 4712−4721.

(4) Duan, H.; Li, D.; Tang, Y.; He, Y.; Ji, S.; Wang, R.; Lv, H.; Lopes, P. P.; Paulikas, A. P.; Li, H.; Mao, S. X.; Wang, C.; Markovic, N. M.; Li, J.; Stamenkovic, V. R.; Li, Y. High-Performance Rh$_2$P Electrocatalyst for Efficient Water Splitting. *J. Am. Chem. Soc.* **2017**, *139*, 5494−5502.

(5) Li, J.; Zhao, Z.; Ma, Y.; Qu, Y. Graphene and Their Hybrid Electrocatalysts for Water Splitting. *ChemCatChem* **2017**, *9*, 1554−1568.

(6) Gong, L.; Ren, D.; Deng, Y.; Yeo, B. S. Efficient and Stable Evolution of Oxygen Using Pulse-Electrodeposited Ir/Ni Oxide Catalyst in Fe-Spiked KOH Electrolyte. *ACS Appl. Mater. Interfaces* **2016**, *8*, 15985−15990.

(7) Cheng, Y.; Jiang, S. P. Advances in Electrocatalysts for Oxygen Evolution Reaction of Water Electrolysis-From Metal Oxides to Carbon Nanotubes. *Prog. Nat. Sci.* **2015**, *25*, 545−553.

(8) Zhu, Y.; Zhou, W.; Yu, J.; Chen, Y.; Liu, M.; Shao, Z. Enhancing Electrocatalytic Activity of Perovskite Oxides by Tuning Cation Deficiency for Oxygen Reduction and Evolution Reactions. *Chem. Mater.* **2016**, *28*, 1691−1697.

(9) Li, L.; Yang, H.; Miao, J.; Zhang, L.; Wang, H.-Y.; Zeng, Z.; Huang, W.; Dong, X.; Liu, B. Unraveling Oxygen Evolution Reaction on Carbon-Based Electrocatalysts: Effect of Oxygen Doping on Adsorption of Oxygenated Intermediates. *ACS Energy Lett.* **2017**, *2*, 294−300.

(10) Long, X.; Wang, Z.; Xiao, S.; An, Y.; Yang, S. Transition Metal Based Layered Double Hydroxides Tailored for Energy Conversion and Storage. *Mater. Today* **2016**, *19*, 213−226.

(11) Bediako, D. K.; Lassalle-Kaiser, B.; Surendranath, Y.; Yano, J.; Yachandra, V. K.; Nocera, D. G. Structure−Activity Correlations in a Nickel−Borate Oxygen Evolution Catalyst. *J. Am. Chem. Soc.* **2012**, *134*, 6801−6809.

(12) Yoshida, M.; Mitsutomi, Y.; Mineo, T.; Nagasaka, M.; Yuzawa, H.; Kosugi, N.; Kondoh, H. Direct Observation of Active Nickel Oxide Cluster in Nickel−Borate Electrocatalyst for Water Oxidation by *In Situ* O K-Edge X-Ray Absorption Spectroscopy. *J. Phys. Chem. C* **2015**, *119*, 19279−19286.

(13) Yuan, C.-Z.; Jiang, Y.-F.; Wang, Z.; Xie, X.; Yang, Z.-K.; Yousaf, A. B.; Xu, A.-W. Cobalt Phosphate Nanoparticles Decorated with Nitrogen-Doped Carbon Layers as Highly Active and Stable Electrocatalysts for the Oxygen Evolution Reaction. *J. Mater. Chem. A* **2016**, *4*, 8155−8160.

(14) Zhao, S.; Li, C.; Huang, H.; Liu, Y.; Kang, Z. Carbon Nanodots Modified Cobalt Phosphate as Efficient Electrocatalyst for Water Oxidation. *J. Materiomics* **2015**, *1*, 236−244.

(15) Zhibin, L.; Chang, Y.; Xiaotong, H.; Juan, Y.; Changtai, Z.; Huawei, H.; Jieshan, Q. CoMn Layered Double Hydroxides/Carbon Nanotubes Architectures as High-Performance Electrocatalysts for the Oxygen Evolution Reaction. *ChemElectroChem* **2016**, *3*, 906−912.

(16) Zhu, X.; Tang, C.; Wang, H.-F.; Zhang, Q.; Yang, C.; Wei, F. Dual-Sized NiFe Layered Double Hydroxides *In Situ* Grown on Oxygen-Decorated Self-Dispersal Nanocarbon as Enhanced Water Oxidation Catalysts. *J. Mater. Chem. A* **2015**, *3*, 24540−24546.

(17) Zhang, J.; Liu, J.; Xi, L.; Yu, Y.; Chen, N.; Sun, S.; Wang, W.; Lange, K. M.; Zhang, B. Single-Atom Au/NiFe Layered Double Hydroxide Electrocatalyst: Probing the Origin of Activity for Oxygen Evolution Reaction. *J. Am. Chem. Soc.* **2018**, *140*, 3876−3879.

(18) Zhan, T.; Zhang, Y.; Liu, X.; Lu, S.; Hou, W. NiFe Layered Double Hydroxide/Reduced Graphene Oxide Nanohybrid as an Efficient Bifunctional Electrocatalyst for Oxygen Evolution and Reduction Reactions. *J. Power Sources* **2016**, *333*, 53−60.

(19) Zhan, T.; Liu, X.; Lu, S.; Hou, W. Nitrogen Doped NiFe Layered Double Hydroxide/Reduced Graphene Oxide Mesoporous Nanosphere as an Effective Bifunctional Electrocatalyst for Oxygen Reduction and Evolution Reactions. *Appl. Catal., B* **2017**, *205*, 551−558.

(20) Gong, M.; Li, Y.; Wang, H.; Liang, Y.; Wu, J. Z.; Zhou, J.; Wang, J.; Regier, T.; Wei, F.; Dai, H. An Advanced Ni−Fe Layered Double Hydroxide Electrocatalyst for Water Oxidation. *J. Am. Chem. Soc.* **2013**, *135*, 8452−8455.

(21) Gong, M.; Dai, H. A Mini Review of NiFe-Based Materials as Highly Active Oxygen Evolution Reaction Electrocatalysts. *Nano Res.* **2015**, *8*, 23−39.

(22) Ma, W.; Ma, R.; Wang, C.; Liang, J.; Liu, X.; Zhou, K.; Sasaki, T. A Superlattice of Alternately Stacked Ni−Fe Hydroxide Nano-

sheets and Graphene for Efficient Splitting of Water. *ACS Nano* **2015**, *9*, 1977−1984.

(23) Tang, D.; Liu, J.; Wu, X.; Liu, R.; Han, X.; Han, Y.; Huang, H.; Liu, Y.; Kang, Z. Carbon Quantum Dot/NiFe Layered Double-Hydroxide Composite as a Highly Efficient Electrocatalyst for Water Oxidation. *ACS Appl. Mater. Interfaces* **2014**, *6*, 7918−7925.

(24) Wang, Q.; Zhou, D.; Yu, H.; Zhang, Z.; Bao, X.; Zhang, F.; Zhou, M. NiFe Layered Double-Hydroxide and Cobalt-Carbon Composite as a High-Performance Electrocatalyst for Bifunctional Oxygen Electrode. *J. Electrochem. Soc.* **2015**, *162*, A2362−A2366.

(25) Julien, C. M.; Massot, M.; Poinsignon, C. Lattice Vibrations of Manganese Oxides: Part I. Periodic Structures. *Spectrochim. Acta, Part A* **2004**, *60*, 689−700.

(26) Cunha, V. R. R.; Petersen, P. A. D.; Gonçalves, M. B.; Petrilli, H. M.; Taviot-Gueho, C.; Leroux, F.; Temperini, M. L. A.; Constantino, V. R. L. Structural, Spectroscopic (NMR IR, and Raman), and DFT Investigation of the Self-Assembled Nanostructure of Pravastatin-LDH (Layered Double Hydroxides) Systems. *Chem. Mater.* **2012**, *24*, 1415−1425.

(27) Louie, M. W.; Bell, A. T. An Investigation of Thin-Film Ni−Fe Oxide Catalysts for the Electrochemical Evolution of Oxygen. *J. Am. Chem. Soc.* **2013**, *135*, 12329−12337.

(28) Wu, S.; Hui, K. S.; Hui, K. N. One-Dimensional Core−Shell Architecture Composed of Silver Nanowire@Hierarchical Nickel−Aluminum Layered Double Hydroxide Nanosheet as Advanced Electrode Materials for Pseudocapacitor. *J. Phys. Chem. C* **2015**, *119*, 23358−23365.

(29) O'Neill, L.; Johnston, C.; Grant, P. S. Enhancing the Supercapacitor Behaviour of Novel Fe_3O_4/FeOOH Nanowire Hybrid Electrodes in Aqueous Electrolytes. *J. Power Sources* **2015**, *274*, 907−915.

(30) Nayak, S.; Parida, K. M. Dynamics of Charge-Transfer Behavior in a Plasmon-Induced Quasi-Type-II $p-n/n-n$ Dual Heterojunction in $Ag@Ag_3PO_4/G-C_3N_4$/NiFe LDH Nanocomposites for Photocatalytic Cr(VI) Reduction and Phenol Oxidation. *ACS Omega* **2018**, *3*, 7324−7343.

(31) Zhou, D.; Cai, Z.; Lei, X.; Tian, W.; Bi, Y.; Jia, Y.; Han, N.; Gao, T.; Zhang, Q.; Kuang, Y.; Pan, J.; Sun, X.; Duan, X. NiCoFe-Layered Double Hydroxides/N-Doped Graphene Oxide Array Colloid Composite as an Efficient Bifunctional Catalyst for Oxygen Electrocatalytic Reactions. *Adv. Energy Mater.* **2018**, *8*, 1701905.

(32) Roemelt, M.; Beckwith, M. A.; Duboc, C.; Collomb, M.-N.; Neese, F.; DeBeer, S. Manganese K-Edge X-Ray Absorption Spectroscopy as a Probe of the Metal−Ligand Interactions in Coordination Compounds. *Inorg. Chem.* **2012**, *51*, 680−687.

(33) Nam, K.-W.; Kim, M. G.; Kim, K.-B. *In Situ* Mn K-Edge X-Ray Absorption Spectroscopy Studies of Electrodeposited Manganese Oxide Films for Electrochemical Capacitors. *J. Phys. Chem. C* **2007**, *111*, 749−758.

(34) Qian, L.; Lu, Z.; Xu, T.; Wu, X.; Tian, Y.; Li, Y.; Huo, Z.; Sun, X.; Duan, X. Trinary Layered Double Hydroxides as High-Performance Bifunctional Materials for Oxygen Electrocatalysis. *Adv. Energy Mater.* **2015**, *5*, 1500245.

(35) Song, F.; Hu, X. Exfoliation of Layered Double Hydroxides for Enhanced Oxygen Evolution Catalysis. *Nat. Commun.* **2014**, *5*, 4477.

(36) Song, F.; Hu, X. Ultrathin Cobalt−Manganese Layered Double Hydroxide Is an Efficient Oxygen Evolution Catalyst. *J. Am. Chem. Soc.* **2014**, *136*, 16481−16484.

(37) Fan, K.; Chen, H.; Ji, Y.; Huang, H.; Claesson, P. M.; Daniel, Q.; Philippe, B.; Rensmo, H.; Li, F.; Luo, Y.; Sun, L. Nickel−Vanadium Monolayer Double Hydroxide for Efficient Electrochemical Water Oxidation. *Nat. Commun.* **2016**, *7*, 11981.

(38) Chala, S. A.; Tsai, M.-C.; Su, W.-N.; Ibrahim, K. B.; Duma, A. D.; Yeh, M.-H.; Wen, C.-Y.; Yu, C.-H.; Chan, T.-S.; Dai, H.; Hwang, B.-J. Site Activity and Population Engineering of NiRu-Layered Double Hydroxide Nanosheets Decorated with Silver Nanoparticles for Oxygen Evolution and Reduction Reactions. *ACS Catal.* **2019**, *9*, 117−129.

(39) Chen, Z.; Yu, A.; Higgins, D.; Li, H.; Wang, H.; Chen, Z. Highly Active and Durable Core−Corona Structured Bifunctional Catalyst for Rechargeable Metal−Air Battery Application. *Nano Lett.* **2012**, *12*, 1946−1952.

(40) Chen, Z.; Yu, A.; Ahmed, R.; Wang, H.; Li, H.; Chen, Z. Manganese Dioxide Nanotube and Nitrogen-Doped Carbon Nanotube Based Composite Bifunctional Catalyst for Rechargeable Zinc-Air Battery. *Electrochim. Acta* **2012**, *69*, 295−300.

(41) Alia, S. M.; Duong, K.; Liu, T.; Jensen, K.; Yan, Y. Supportless Silver Nanowires as Oxygen Reduction Reaction Catalysts for Hydroxide-Exchange Membrane Fuel Cells. *ChemSusChem* **2012**, *5*, 1619−1624.

(42) Yu, L.; Zhou, H.; Sun, J.; Qin, F.; Yu, F.; Bao, J.; Yu, Y.; Chen, S.; Ren, Z. Cu Nanowires Shelled with NiFe Layered Double Hydroxide Nanosheets as Bifunctional Electrocatalysts for Overall Water Splitting. *Energy Environ. Sci.* **2017**, *10*, 1820−1827.